Study on the Transient Absorption Spectroscopy of a D-π-A Structure Aggregation-Induced Emission Luminogen and Its Photodynamic Therapy Application

Si-Wei Zhang,[a,&] Junqiao Wang,[b,&,] Zaiyu Wang,[a,&] Ming Shao,[c] Chen Zhang,[d] Jianwei Sun,[a] Jacky, W. Y. Lam,[a*] and Ben Zhong Tang[a,e,*]

[a] Department of Chemistry, Hong Kong Branch of Chinese National Engineering Research Center for Tissue Restoration and Reconstruction, Division of Life Science and State Key Laboratory of Molecular Neuroscience, The Hong Kong University of Science and Technology, Kowloon 999077, Hong Kong, China

[b] Open FIESTA, Shenzhen International Graduate School, Tsinghua University, Shenzhen, 518055, China.

[c] Department of Central Laboratory, the Second Affiliated Hospital, School of Medicine, The Chinese University of Hong Kong, Shenzhen & Longgang District People's Hospital of Shenzhen, Shenzhen, 518172, China

[d] The State Key Laboratory of Chemical Oncogenomics, Shenzhen International Graduate School, Tsinghua University, Shenzhen, 518055, China

[e] School of Science and Engineering, Shenzhen Institute of Aggregate Science and Technology, The Chinese University of Hong Kong, Shenzhen (CUHK-Shenzhen), Guangdong 518172, P.R. China

& These authors are equally contributed.

* Corresponding author E-mail: chjacky@ust.hk (Prof. J.W.Y. Lam); and tangbenz@cuhk.edu.cn (Prof. B.Z. Tang)

Abstract

Photodynamic therapy (PDT) represents an emerging and noninvasive modality that has gained clinical approval for the treatment of cancers, leveraging photosensitizers for optimal therapeutic efficacy. In this study, we synthesized a photosensitizer (denoted as DTCSPP) exhibiting a donor-π-acceptor (D-π-A) structural motif. The DTCSPP manifests aggregation-induced emission (AIE) characteristics, along with good biocompatibility and mitochondrial targeting capabilities attributed to its intrinsic charge and D-π-A architecture. The excited-state intramolecular charge transfer of DTCSPP was systematically investigated in both solution and aggregate states using femtosecond transient absorption spectroscopy (fs-TA). The fs-TA results revealed that DTCSPP exhibited a more rapid and facile excited-state molecular motion in the solution state compared to the aggregate state, implying the predominance of nonradiative decay in its photophysical processes within the solution. Given its ability to simultaneously generate type I and type II reactive oxygen species and induce ferroptosis and autophagy in cancer cells, DTCSPP demonstrates effectiveness in PDT at both cellular and in *vivo* levels. This study contributes a comprehensive understanding of the excited-state intramolecular charge transfer dynamics of charged D-π-A type AIE photosensitizers, shedding light on their potential application in PDT. The multifaceted capabilities of DTCSPP underscore its promise in advancing the field of anticancer therapeutics, providing valuable insights for the identification of anticancer targets and the development of novel drugs.

Keywords

Aggregation-induced emission; Photosensitizer; Photodynamic therapy; Reactive oxygen species; Transient absorption spectroscopy

1. Introduction

Photodynamic therapy (PDT) has emerged as a noninvasive therapeutic modality, garnering clinical approval for cancer treatment since its initial success in managing bladder cancer in 1976.[1],[2] Effective PDT relies on three essential elements: photosensitizer, oxygen and Light. The photosensitizer enriched in the tumor site can be actived by the light, and the relaxation process of electrons from the lowest unoccupied molecular orbital (LUMO) to the highest occupied molecular orbital (HOMO) is accompanied by generating the reactive oxygen species (ROS), leading to localized cell death and tissue devastation. Photosensitizers can be divided into two categories based on their mechanism of action. The type I photosensitizers can react directly with the substrate by electron transfer to produce ROS like superoxide anion radical ($\cdot O_2^-$), a hydroxyl radical ($\cdot OH$), and hydrogen peroxide (H_2O_2). In comparison, type II photosensitizers can react with molecular oxygen to form singlet oxygen ($^1O_2$) by energy transfer.[3] Photosensitizers, possessing high biocompatibility and remarkable ROS generation efficiency, play a crucial role in the successful implementation of PDT treatment.

Aggregation-induced emission luminogens (AIEgens) typically show weak fluorescence or nonfluorescence in the solution state but enhanced emission in the aggregate form.[4] AIEgens generally possess large Stokes' shift, good biocompatibility, and great luminosity, which have been certificated to have great potential in biosensing,[5] imaging,[6] anticancer,[7] anti-infective,[8] and photoelectronic devices applications.[9] Several AIE moieties, such as tetraphenylethylene (TPE), siloles, and cyanostilbenes, were reported.[10] Photosensitizers with AIE (AIE-PS) features are particularly promising in PDT treatment. Among them, the donor-π-acceptor (D-π-A) structure AIE-PSs adopt the intramolecular charge transfer strategy to separate the HOMO and the LUMO, which facilitates intersystem crossing (ISC) process from the lowest singlet state (S_1) to the lowest triplet state (T_1) and enhances the ROS generation.[11] Additionally, the reduced energy gap between S_1 and T_1 (ΔE_{st}) in aggregates results from strong D-A interactions.[12] Charged AIE-PSs exhibit enhanced

proximity in three-dimensional space due to electrostatic interactions between positively charged AIEgens and negatively charged biological species, suppressing nonradiative transitions.[13] Besides, the charged AIE-PSs inherit better water solubility and they are easier to target organelles such as mitochondria.[14] Yin et al. reported a readily synthesized AIEgen TPA-Pyr-BP, which employs a strong electron acceptor of pyridinium and an electron donor of triphenylamine, proved an elevated electron D-A interaction and intramolecular charge transfer behavior.[15] Chen et al. reported two mitochondria-targeted AIE-PSs (DTCSPY and DTCSPE) with charged D-π-A structures. DTCSPY employs a comparatively rigid alkyne group capable of hindering the nonradiative transition due to intramolecular motion and exhibits a better PDT for HT22 neuron cells.[16] Hasrat et al. disclosed that a series of charged D-π-A AIE-PSs displayed superior photosensitivity for active HepG2 cells and sensitively detecting lipid droplets.[17] Although many such structure AIE-PSs have been reported and applied to diversiform bioapplication,[14b, 15-18] the intramolecular charge transfer in the excited states is still insufficiently studied due to the ultrafast excited state relaxation process. To design novel and effective AIE-PSs, detailed research on the excited states of charged D-π-A AIE-PSs is impending.

In this work, a twisted skeleton AIEgen (labeled as DTCSPP) with a charged D-π-A structure is synthesized. Our exploration of the relaxation process of excited states harnessed the precision of femtosecond transient absorption spectroscopy (fs-TA), unraveling the intricacies of intramolecular charge transfer. Distinctly, the solution state exhibited a swifter and more facile excited-state molecular motion than its aggregate counterpart, highlighting the preeminence of nonradiative decay in the photophysical processes of DTCSPP in the solution state. Complementary verification through electron paramagnetic resonance (EPR) measurements and fluorescent indicators confirmed the dual capability of DTCSPP in generating both type I ($^1O_2$) and type II ($\cdot O_2$ and $\cdot OH$) free radicals. DTCSPP showcased good mitochondrial targeting and demonstrated its efficacy in PDT at both cellular and in *vivo* levels for MDA-MB-231 cells. This inquiry not only advances our comprehension of the intramolecular charge

transfer dynamics inherent in charged D-π-A structure AIE-PSs but also elucidates their potential in pushing the frontiers of PDT applications.

2. Materials and methods

2.1 Material

DTCSPP was synthesized as the method our group previously reported. The solvents were purchased from Macklin. The 2', 7'-dichlorodihydrofluorescein diacetate (DCF-DA) and MitoTracker Deep Red FM were purchased from Invitrogen. Cell culture medium, phosphate-buffered saline (PBS), fetal bovine serum (FBS), and penicillin-streptomycin solution (PS) were purchased from Gibco. Anti-LC3B antibody, anti-GPX4 antibody, anti-P62 antibody, and anti-β-actin antibody were purchased from Abcam. All materials and reagents were used as received.

2.2 Measurement

The UV-Vis absorption and photoluminescence spectra were recorded on a UV-1900I spectrophotometer (Shimadzu, Japan) and FLS1000 spectrofluorimeter (Edinburgh Instruments, U.K.) at room temperature. The particle size was measured by ZEN3700. (Zetasizer, UK). The electron paramagnetic resonance (EPR) measurements were carried out with a Bruker Model A300 spectrometer (Bruker, America) with 1 G field modulation, 20 mW and 100 G-scan range. The TEMP and DMPO (100 mM) were used as spin-trapping adducts to detect the $^1O_2$ and $\cdot O_2^-$/·OH produced by DTCSPP (0.1 mg/ml) under dark and irradiation, respectively. The TEMP/$^1O_2$ and DMPO/$\cdot O_2^-$ DMPO/· O.H. signals were detected in water and dimethyl sulfoxide, respectively. The femtosecond transient absorption measurements were performed on a Helios (Ultrafast systems) spectrometer using a regeneratively amplified femtosecond Ti: sapphire laser system (Spitfire Pro-F1KXP, Spectra-Physics; frequency, 1 kHz; max pulse energy, 8 mJ; pulse width, 120 fs) at room temperature. Finally, analyze the data through commercial software (Surface Xplorer, Ultrafast Systems).

2.3 Theoretical calculation

DTCSPP was fully optimized by the density functional theory (DFT) method by using CAM-B3LYP density functional and 6-31G (d,p) basis set with Gaussian 16

program. Time-dependent density functional theory (TD-DFT) was carried out at the same level of theory to calculate energy levels of singlet-triplet states and their gap (ΔE_{st}).

2.4 Cell culture

MDA-MB-231 cells are human adherent breast cancer cells, which were obtained by the Chinese Academy of Sciences Cell Banks (Shanghai, China) and were cultured in Leibovitz's L-15 Medium with 10% fetal bovine serum (FBS) in the humidified atmosphere at 37°C without CO_2. The cellular uptakes of DTCSPP were observed in MDA-MB-231 cells by CLSM. About 1×10^5 MDA-MB-231 cells were seeded in a confocal dish and cultured in Leibovitz's L-15 Medium for 24 h. After fully attached, the cells were incubated for 1 h with 5 μM DTCSPP and then imaged by a confocal laser scanning microscope.

2.5 *In vitro* cell viability

Cell viability was measured using human breast cancer cell line MDA-MB-231 by CCK-8 assay. Each group of cancer cells was seeded at cell density of 1×10^4 per well in a 96-well cell culture plate with Leibovitz's L-15 Medium (200 μL). After 24 h, the culture medium need to be replaced by the medium with a final concentration of DTCSPP at 0 to 10 μM. After a 48-hour incubation, the cells were washed with PBS, and then CCK8 (10 μL in 90 μL medium) was addedl. Then, cells were incubated for 2 h and can be measured by the microplate reader at a wavelength of 450 nm.

2.6 Intracellular ROS level

In intracellular ROS generation was evaluated by employing DCFH-DA as the fluorescent indicator. MDA-MB-231 cells were planted onto 35-mm confocal dishes at a density of 1×10^5 cells. After incubation for 24 h, all the medium can be removed and washed with PBS three times. Then, MDA-MB-231 cells were incubated with 10 μM DTCSPP for 1 h and then washed with PBS three times. Then, the cells were incubated with the fluorescent probe DCFH-DA (20 μM) for 30 min at the temperature of 37 °C in the dark and washed three times with PBS. The cells were subsequently treated with a white LED irradiation (50 mW/cm^2) for 2 h and were successively examined by the

CLSM (excited at 488 nm).

2.7 Western blots analysis

Briefly, MDA-MB-231 cells were collected and lysed using lysis buffer at 6 h post different treatments. Then, the extracted proteins were separated through gel electrophoresis (according to their sizes) using 10% sodium dodecyl sulfatepolyacrylamide gel electrophoresis (SDS-PAGE). Next, these proteins were transferred from the gel to PVDF membranes (Millipore, Billerica, MA, USA). After that, the membrane containing protein bands was incubated with a blocking buffer containing 5% BSA for 0.5 h. After that, membrane was incubated with primary antibody for 2 h, then incubated with HRP-conjugated secondary antibody for 1 h post three-times washing by 1×PBST. Finally, the related protein bands were visualized using Tanon-5200 Chemiluminescent Imaging System (Tanon Science and Technology) after washing.

2.8 *In vivo* anticancer studies

The BALB/c nude mice (female, 4 weeks) were obtained from Guangdong Medical Laboratory Animal Center (Guangdong, China) and were raised to 6 weeks old to construct xenografts. All animal experiments were conducted strictly according to the guidelines and approval of the Institutional Animal Care and Use Committee of Shenzhen International Graduate School, Tsinghua University, and the Medical Laboratory Animal Center of Guangdong. China (License No.35 (year 2022). Mice were subcutaneously injected with MDA-MB-231 (1×10^7 cells) and were randomly divided into four groups with 3 mice in each group. Group I: PBS injection without irradiation; Group II: PBS injection with irradiation; Group III: DTCSPP injection without irradiation; Group V: DTCSPP injection with irradiation. After intratumoral injection, a white LED light (150 mW/cm^2) treatment was performed on Group II and Group V by irradiating the tumor region for 20 min every other day. The effect of the different treatment groups was monitored by measuring tumor size and mice body weight for 15 days after PDT treatment. The tumor volume is calculated using the formula as follows:

$$V(mm^3) = \frac{\pi}{6} \times length(mm) \times width(mm) \times height(mm)$$

After 15 days, the tumors of the mice were dissected and weighed.

2.9 Statistical Analysis

Mean ± standard deviation (S.D.) was used for quantitative data analysis. Statistical comparisons were analyzed by one-way ANOVA with a Tukey post-hoc test and unpaired Student's t-test (two-tailed). $*P < 0.05$ means a statistically significant difference. $**P < 0.01$ and $***P < 0.001$ mean highly significant.

3. Results and discussions

3.1 Photophysical properties of DTCSPP

Figure 1a delineates the molecular structure of the AIE-PS DTCSPP with a typical D-π-A structure. Within this structure, the *N, N*-diphenylthiophen-2-amine and 1-propylpyridin-1-ium groups serve as the donor and acceptor moieties, respectively. Bridging these components are benzene and a relatively rigid alkyne group, forming a twisted skeleton. Notably, a positive charge is localized on the pyridine nitrogen. To unravel the photophysical attributes of DTCSPP, a comprehensive analysis was conducted employing UV-VIS absorption and photoluminescence (PL) spectroscopy. As shown in Figure 1b and Figure S1, DTCSPP exhibits a noticeable solvent effect due to its D-π-A structure. In dimethyl sulfoxide (DMSO), the absorption peak manifests at 497 nm, while in dioxane and dichloromethane (DCM), the peaks shift to 441 nm and 531 nm, respectively. The PL peak symmetry centers around 560 nm in DMSO, dioxane, and acetone, exhibiting redshifts and broadening in tetrahydrofuran (THF) and DCM. Delving further into the AIE characteristics of DTCSPP in varying DMSO and water fractions (f_{water}) in Figure 1c-d, it is evident that the fluorescence intensity in pure DMSO is relatively subdued. However, with an increase in f_{water}, the PL intensity experiences an enhancement accompanied by a redshift. Transitioning to a DMSO: water ratio of 1:9 prompts the formation of DTCSPP aggregate nanoparticles with a discernible particle size of 119 nm (Figure S2). The relative fluorescence intensity ($\alpha_{AIE} = I/I_0$) registers a remarkable twenty-fold enhancement.

Moreover, in the solid state, a 2% concentration of DTCSPP within a polymethyl methacrylate (PMMA) film exhibits intensified emission at 680 nm, as elucidated through time-resolved photoluminescence (TRPL) with a characteristic decay time of 17 ns, markedly surpassing its solution state counterpart (Figure S3). The heightened fluorescence intensity and prolonged lifetime observed in the aggregate state signify the mitigation of nonradiative transitions attributed to molecular motion.

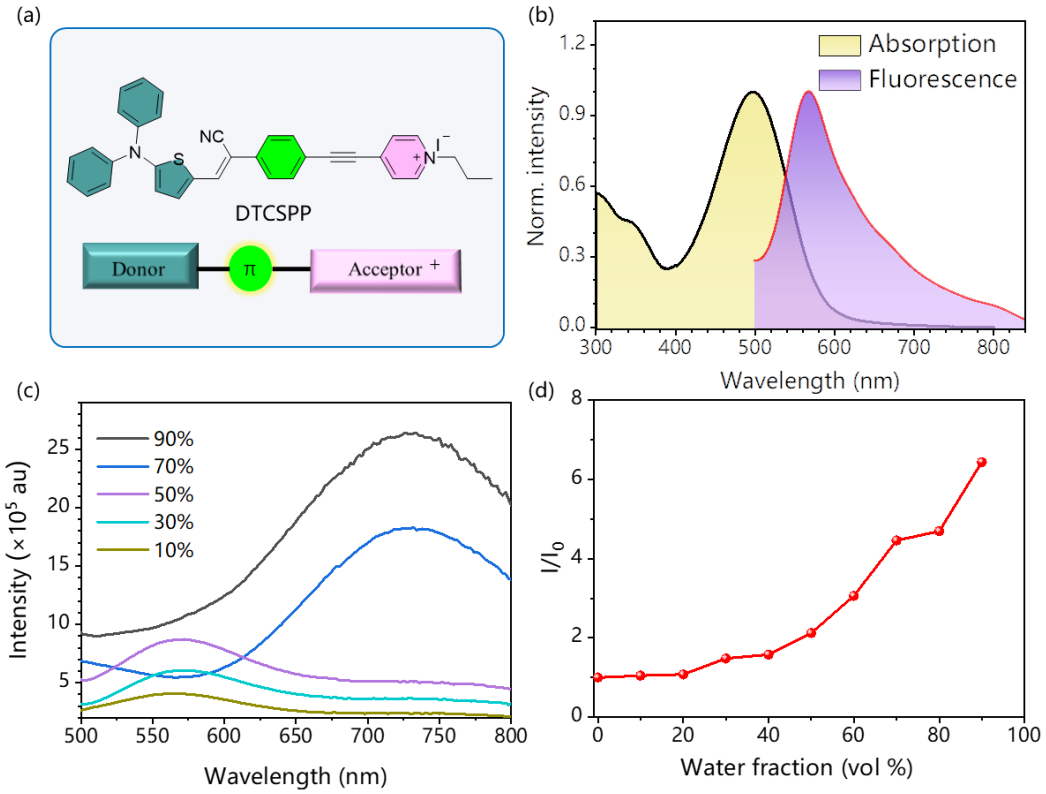

Figure 1. (a) The molecular structure of the DTCSPP. (b) Normalized absorption and photoluminescence spectra of the DTCSPP in DMSO solution. Concentration = 10^{-5} M. (c) Fluorescence intensities of DTCSPP in DMSO/water mixtures with different water fractions (f_{water}). Concentration = 10^{-5} M, λ_{ex} = 500 nm. (d) The plot of relative PL intensity ($\alpha_{AIE} = I/I_0$) of DTCSPP in mixtures of DMSO/water with different f_{water} (vol %)

3.2 Theoretical calculation and femtosecond transient absorption spectra

To gain deeper insights into the molecular structure and excited properties of DTCSPP, a Density Functional Theory (DFT) analysis was conducted. Figure S4 and Figure 2a present the optimized geometries and electron cloud distribution. Specifically, the optimized geometry illustrates a pronounced dihedral angle within the stilbene

segment, measuring 17.8°. Simultaneously, the HOMO and LUMO electron clouds exhibit a discernible spatial separation in DTCSPP. The HOMO electron cloud primarily localizes on the N, N-diphenylthiophen-2-amine moiety, whereas the LUMO electron cloud is prominently situated on the 1-propylpyridin-1-ium group. This spatial distribution implies a distinct intramolecular charge transfer excited feature within DTCSPP, accentuating its propensity for dynamic electronic transitions.

Femtosecond transient absorption spectroscopy (fs-TA) with the pump-probe system can monitor the evolution of the molecular excited states at the femtosecond scale. Here, a 400 nm pump laser pulse was applied to excite the DTCSPP in both the DMSO solution state and aggregate state (mixture of DMSO: water = 1:9) (concentration = 10^{-5} M) to study the influence of aggregation behavior on excited states. The time-wavelength-dependent fs-TA color map (Figure 2b and Figure 2f) provides a detailed depiction of the dynamic evolution of molecular excited states. The negative induced optical density (OD) observed around 450 nm corresponds to the Stimulated Emission (SE) band, while the positive OD peak around 590 nm indicates Excited State Absorption (ESA). The SE process elucidates the sample's return to the ground state from an unstable excited state under the pump laser, accompanied by fluorescence generation. Meanwhile, ESA directly mirrors the internal conversion of $S_n \rightarrow S_1$ and the molecular structural alterations during the excitation process.

In the solution state, the evolution of the ESA peak from 50 to 900 fs, marked by a redshift from 480 nm to 602 nm (Figure 2c-d), is attributed to a molecular motion process, such as the torsion of the molecular skeleton and rotation of the benzene ring. The rotation of the molecular skeleton under Light induces a redshift in the absorption peak of the excited state.[19] Notably, the kinetic fitting result at 590 nm reveals a lifetime of 53.2 ps. In the aggregate state, the ESA peak evolution spans from 50 to 1200 fs, with a redshift from 486 nm to 605 nm (Figure 2g-h), surpassing the extent observed in the solution state. The corresponding kinetic fitting result at 590 nm indicates a sluggish lifetime of 72.8 ps (Figure 2i). This comparative analysis suggests that the solution state exhibits a faster and more facile excited-state molecular motion

than the aggregate state, indicating the predominant role of nonradiative decay in the photophysical processes of DTCSPP. The aggregate state, conversely, effectively inhibits molecular motion.

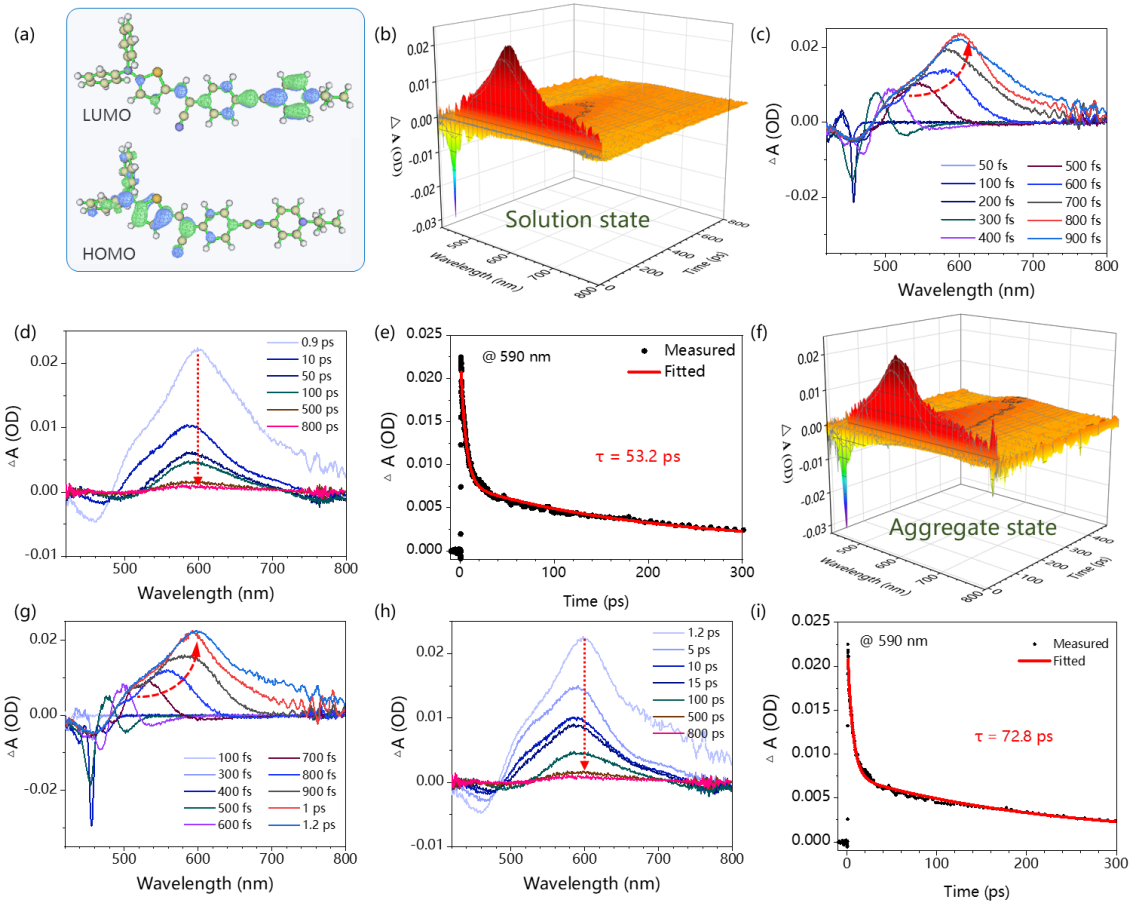

Figure 2. (a) The DFT simulated electron cloud distributions of HOMO and LUMO at CAM-B3LYP density functional and 6-31G(d,p) basis set. The fs-TA of DTCSPP in DMSO solution: (b) The time-wavelength-dependent color maps, (c-d) the select fs-TA spectra. (e)The kinetic fitting of peaks at 590 nm. The fs-TA of DTCSPP in the mixture of DMSO: water = 1:9 (f) The time-wavelength-dependent color maps, (g-h) the select fs-TA spectra. (i)The kinetic fitting of peaks at 590 nm. Concentration = 10^{-5} M. The pump laser is 400 nm.

3.3 ROS generation

The electron paramagnetic resonance (EPR) measurement was carried out to assess the generation of the ROS. Spin-trap agent 5,5-dimethyl-1-pyrrolinr-N-oxide (DMPO) and 4-amino-2,2,6,6-tetramethylpiperidine (TEMP) were adopted to trap the radical of $\cdot OH/\cdot O_2^-$ and $^1O_2$, respectively. As illustrated in Figure 3a-c, no discernible EPR signal was detected under dark conditions. In stark contrast, under light exposure,

distinct EPR spectra corresponding to different capture agents emerged, unequivocally confirming the generation of diverse free radicals. The sharp and strong intensity of the EPR spectra attests to the high efficiency of ROS generation facilitated by DTCSPP. Furthermore, fluorescent indicators were adopted to detect the intensity of free radical generation. Indicators 9,10-anthracenedivl-bis (methylene) dimalonic acid (ABDA) and hydroxyphenyl fluorescein (HPF) were then utilized for the detection $^1O_2$ and ·OH, respectively. In comparison to the commercial photosensitizer Rose Bengal (RB), DTCSPP exhibited superior $^1O_2$ generation efficiency, as elucidated in Figure 3d and Figure S6. The relative PL intensity I/I_0 in HPF and 2,7-dichlorodihydrofluorescein diacetate (DCFH) also experienced a substantial increase of 15 times and 400 times, respectively (Figure 3e-f and Figure S7). This noteworthy enhancement in effective ROS generation efficiency underscores the potential of DTCSPP for achieving exemplary performance in PDT. The intricate interplay between DTCSPP and various indicators unveils its capacity for robust ROS generation, positioning it as a promising candidate for efficient PDT treatments.

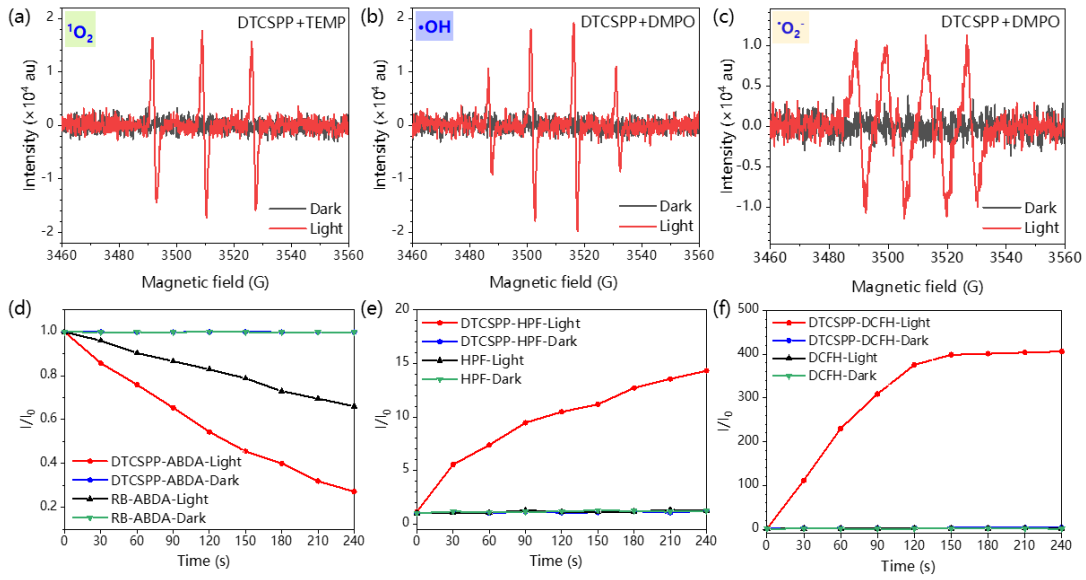

Figure 3. EPR spectra of (a) $^1O_2$ trapped by TEMP, (b)· OH, and (c)·O_2^- trapped by DMPO and with and without laser irradiation. The plot of relative PL intensity of (d) ABDA (for $^1O_2$ detection), (e) HPF (for ·OH detection), and (f) DCFH in the presence of 1 uM DTCSPP or Rose Bengal (RB) upon white light irradiation for 1 min.

3.4 Intracellular ROS detection and PDT treatment

The DTCSPP can be taken up by MDA-MB-231 cells (Figure S8), so intracellular ROS generation can be detected utilizing a DCFH probe. Figure 4a-d vividly illustrates that MDA-MB-231 cells subjected to PBS-only, PBS+Light, and the DTCSPP-only groups exhibited negligible green fluorescence signals, indicative of a lack of ROS generation within the cellular milieu. In contrast, MDA-MB-231 cells treated with DTCSPP followed by white light irradiation displayed a pronounced green fluorescence. The quantification of relative fluorescence intensity, as depicted in Figure 4e, unequivocally establishes that the DTCSPP + Light group manifests the strongest green fluorescence, underscoring its good intracellular ROS production capacity.

The standard Cell Counting Kit-8 (CCK8) assay is also conducted using MDA-MB-231 cells to demonstrate DTCSPP cell-killing performance. As shown in Figure 4f, under dark conditions, the cells showed good viability under the treatment of different concentrations of DTCSPP. Even at the concentration of 10 uM, almost 100% viability was guaranteed, while under light conditions, a notable decline in cell viability was observed even at lower concentrations, with 5 μM yielding less than 10% viability. Moreover, it can be estimated that the Half-maximal inhibitory concentration (IC_{50}) of DTCSPP is about 2.5 μM under Light, highlighting its good intracellular ROS generation capability. This comprehensive analysis underscores not only the good intracellular ROS-generating potential of DTCSPP but also its consequential impact on cell viability under light conditions.

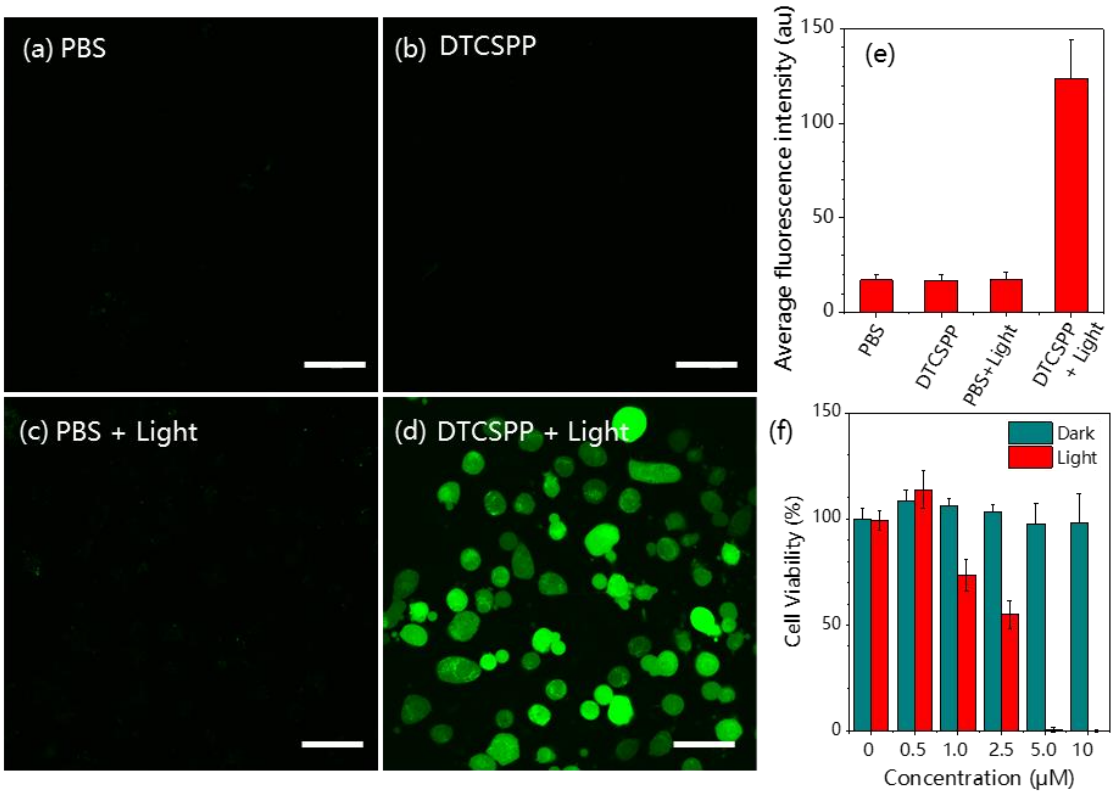

Figure 4. MDA-MB-231 cells intracellular ROS detection by DCFH probe under (a) PBS only, (b) PBS + light, (c)DTCSPP only, and (d) DTCSPP + light. (e) Quantitative analysis of Figure 4a-d using ImageJ software (n = 3 for each group). (f) Cell viability of MDA-MB-231 cells after treatment with various formulations. Scale bar: 50 μm. White light intensity 50 mW/cm^2.

The mitochondria-targeting ability of DTCSPP was assessed through co-staining with the commercial mitochondrial probe Mito-Tracker Deep Red. As depicted in Figure 5a-c, the co-localization of the red emission from Mito-Tracker Deep Red and the green emission from DTCSPP demonstrated a high overlap, yielding a Pearson's correlation coefficient of 0.68. This result substantiates the good mitochondria-targeting capability of DTCSPP, further strengthening its potential as an effective therapeutic agent. Observing the morphological characteristics of MDA-MB-231 cells under various treatments, cells subjected to PBS, PBS + Light, and DTCSPP only retained a spindle-shaped morphology (Figure 5d-g). Remarkably, cells treated with DTCSPP + Light exhibited a distinct rounding, with no observable membranous tissue rupture. This morphological alteration underscores the impact of DTCSPP in inducing structural changes in cancer cells. To delve deeper into the anti-tumor mechanisms of

DTCSPP, a Western blot experiment was conducted, focusing on glutathione peroxidase (GPX4), LC3B, and P62 proteins, representative markers of ferroptosis and autophagy. As illustrated in Figure 5h-i, quantitative analysis revealed a significant downregulation of GPX4 and LC3B expression in the DTCSPP + Light group. This inhibition suggests that ferroptosis and autophagy pathways may contribute to cancer cell death induced by DTCSPP.

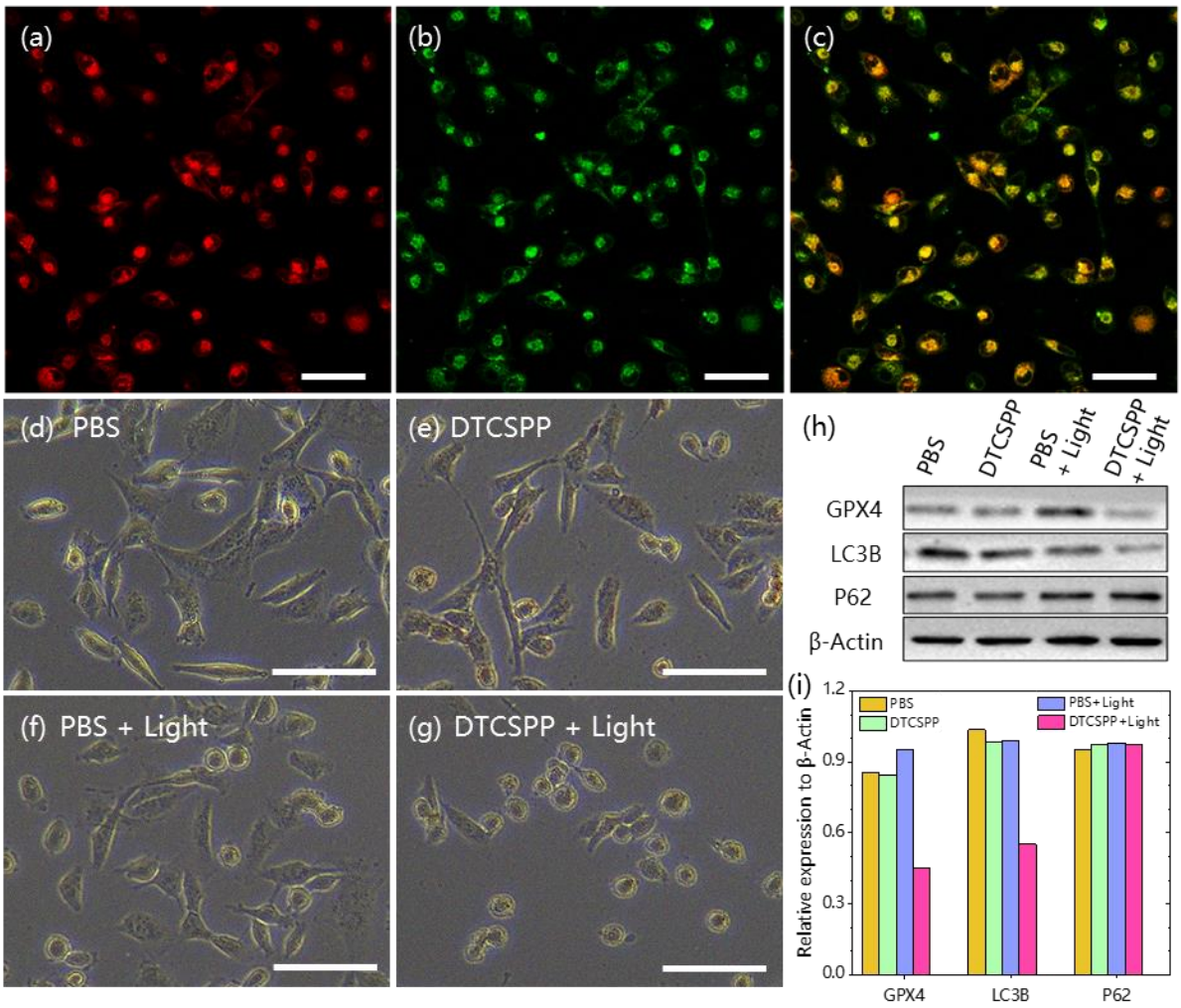

Figure 5. Microscopy images of co-localization between (a) 5 μM DTCSPY and (b) 1 μM MTDR in MDA-MB-231 cells; (c) overlap between a and b; The MDA-MB-231 cells morphology after (d) PBS, (e) DTCSPP, (f) PBS+Light, and (g) DTCSPP+Light treatment. Scale bar: 100 μm. (h) The mechanism analysis of cytoprotective autophagy and ferroptosis with different treatments by western blots. (i) Quantitative analysis of GPX4, LC3B, and P62 dots in different groups.

3.5 In vivo anticancer studies

To assess the in vivo performance of the DTCSPP, a tumor-bearing mouse model was meticulously established. Six-week-old female nude mice were subcutaneously injected with a cell suspension containing 1×10^7 MDA-MB-231 cells. The tumor volume was allowed to reach approximately 100 mm^3 before initiating the in vivo experiment. Subsequently, the mice (n = 3) underwent intratumoral injection with PBS or DTCSPP (10 mg/kg) accompanied by white LED light irradiation (150 mW/cm^2) for 2 hours or without irradiation. As illustrated in Figure 6a-b and Figure S9, DTCSPP exhibited minimal anti-tumor effects in the absence of light stimulation, with tumor volumes and weights escalating more than six-fold after 15 days, akin to the control groups. However, under irradiation, the tumor inhibition effect was evident, resulting in nearly complete suppression of tumor growth owing to the heightened light-induced ROS production efficiencies of DTCSPP. Figure 6c-d visually and quantitatively depicts the tumor weights following different treatments. Notably, throughout the entire PDT study, there was no noticeable change in body weight (Figure S10), reaffirming the low dark toxicity of DTCSPP.

The mice were sacrificed on day 15 after PDT treatment, and the tumor tissues were collected for histological analysis (Figure 6e). All groups exhibited marked nucleus dissociation and necrosis in hematoxylin and eosin (H&E) stain, validating the effective PDT efficacy of the compounds. Collectively, these comprehensive data unequivocally establish DTCSPP's good anti-tumor effects and low biotoxicity in an in vivo setting, highlighting its potential as an impactful and safe therapeutic agent for cancer treatment.

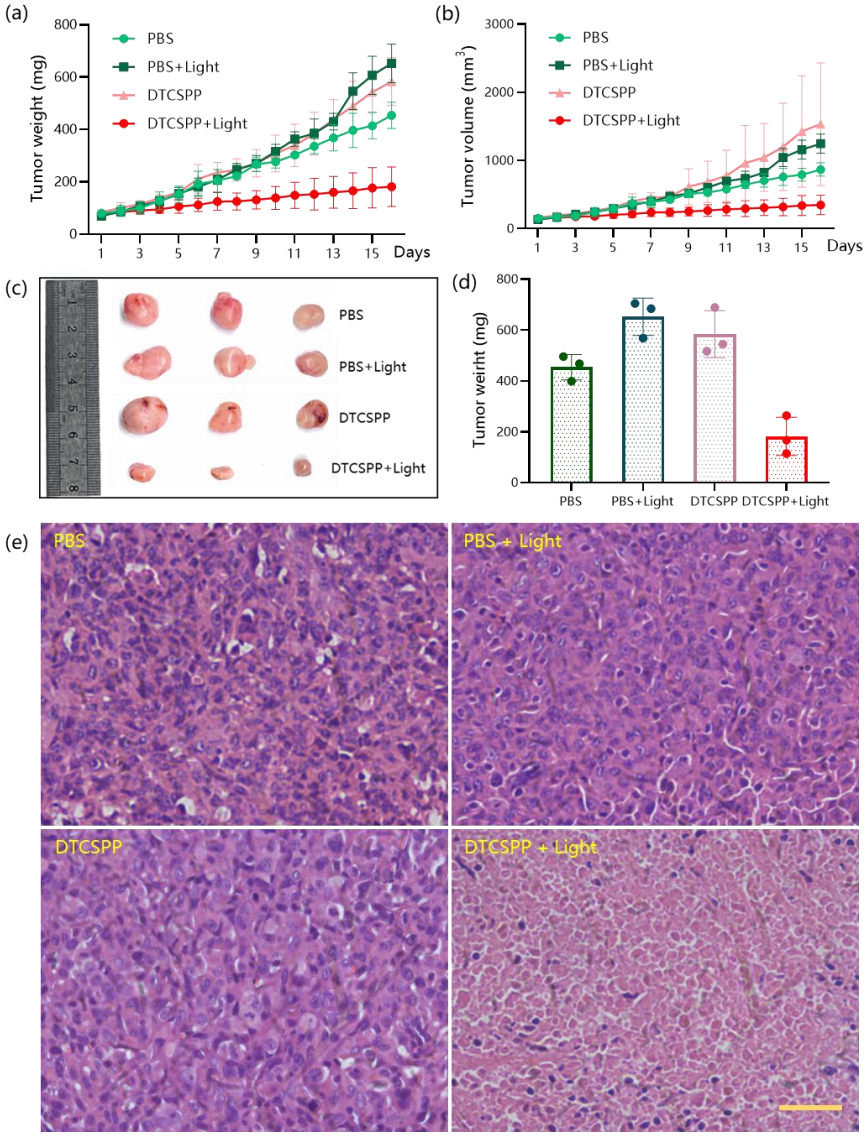

Figure 6 In *vivo* PDT performance of DTCSPP on MDA-MB-231 tumor-bearing mice. (a) tumor weight and (b) tumor volume during the treatment. (c) Tumor images and (d) tumor weight in different groups were obtained on the 14th day after different treatments. (e) H&E staining of tumor tissue in various treatment groups. Scale bar: 200 μm.

4. Conclusions

In summary, we synthesized one AIE-PS with an excellent ability to generate both type I and Type II ROS. With the D-π-A structure and intrinsic charge, the AIE-PS demonstrates good biocompatibility and mitochondrial targeting. We studied the charge transfer process of the excited state in solution and aggregate state by fs-TA and certified that the nonradiative transition dominated the excited state in the solution state and was inhibited in the aggregation state. Benefits of its high ROS generation capacity,

DTCSPP has achieved good anti-tumor effects at both cellular and in *vivo* levels, and the mechanistic underpinnings of its anti-tumor efficacy potentially involve ferroptosis and autophagy. Our discovery provides a deeper comprehension of intramolecular charge transfer processes in excited states, gleaned from fs-TA, coupled with an understanding of how the aggregation state limits intramolecular motion, collectively propels the advancement of AIE-PSs in the realm of therapeutic development. This discovery not only enriches our knowledge of AIE-PSs but also lays a foundation for further exploration and innovation in the field.

Supporting information

The supporting information is available online. Data will be made available on request.

Conflict of interest

The authors declare that they have no known competing financial interests or personal relationships that could have appeared to influence the work reported in this paper.

Acknowledgments

The authors thank the support of the Shenzhen Key Laboratory of Functional Aggregate Materials (ZDSYS20211021111400001), the Science Technology Innovation Commission of Shenzhen Municipality (GJHZ20210705141810031), the Innovation and Technology Commission (ITC-CNERC14SC01 and ITCPD/17-9). We thank the Materials Characterization and Preparation Center, The Chinese University of Hong Kong, Shenzhen, for the material characterization.

References

[1] D. L. Sai, J. Lee, D. L. Nguyen, Y. P. Kim, *Exp Mol Med* **2021**, *53*, 495-504.

[2] J. F. Kelly, M. E. Snell, *J Urol* **1976**, *115*, 150-151.

[3] L. Zhang, D. Ding, *View* **2021**, *2*.

[4] aH. Wang, E. Zhao, J. W. Y. Lam, B. Z. Tang, *Materials Today* **2015**, *18*, 365-377; bY. Tu, Z. Zhao, J. W. Y. Lam, B. Z. Tang, *Matter* **2021**, *4*, 338-349; cZ. Zhao, H. Zhang, J. W. Y. Lam, B. Z. Tang, *Angew Chem Int Ed Engl* **2020**, *59*, 9888-9907.

[5] Y. Yu, S. W. Zhang, J. Jiang, F. Ma, R. Wang, T. Huang, J. Zhao, C. He, G. Wei, *Advanced Sensor Research* **2023**.

[6] R. Zhang, P. Shen, Y. Xiong, T. Wu, G. Wang, Y. Wang, L. Zhang, H. Yang, W. He, J. Du, X. Wei, S. Zhang, Z. Qiu, W. Zhang, Z. Zhao, B. Z. Tang, *National Science Review* **2023**.

[7] D. Yan, Y. Qin, S. Yan, P. Sun, Y. Wang, D. Wang, B. Z. Tang, *Particuology* **2023**, *74*, 103-118.

[8] Y. Wu, J. Li, Z. Shen, D. Wang, R. Dong, J. Zhang, Y. Pan, Y. Li, D. Wang, B. Z. Tang, *Angewandte Chemie* **2022**, *134*.

[9] aS. Zhang, Z. Li, J. Li, B. Wang, F. Chen, X. Li, S. Liu, J. W. Y. Lam, G. Xing, J. Li, Z. Zhao, F. Kang, G. Wei, B. Z. Tang, *Aggregate* **2023**; bY. Zhao, L. Zhang, Y. Liu, Z. Deng, R. Zhang, S. Zhang, W. He, Z. Qiu, Z. Zhao, B. Z. Tang, *Langmuir* **2022**, *38*, 8719-8732; cX. Y. He, H. L. Xie, L. R. Hu, P. C. Liu, C. H. Xu, W. He, W. T. Du, S. W. Zhang, H. Xing, X. Y. Liu, H. Park, T. S. Cheung, M. H. Li, R. T. K. Kwok, J. W. Y. Lam, J. Lu, B. Z. Tang, *Aggregate* **2023**, *4*.

[10] Z.-L. Gong, X. Zhu, Z. Zhou, S.-W. Zhang, D. Yang, B. Zhao, Y.-P. Zhang, J. Deng, Y. Cheng, Y.-X. Zheng, S.-Q. Zang, H. Kuang, P. Duan, M. Yuan, C.-F. Chen, Y. S. Zhao, Y.-W. Zhong, B. Z. Tang, M. Liu, *Science China Chemistry* **2021**.

[11] I. R. Gould, *The Journal of Physical Chemistry A* **2003**, *107*, 3515-3524.

[12] T. Zhang, J. Zhang, F. B. Wang, H. Cao, D. Zhu, X. Chen, C. Xu, X. Yang, W. Huang, Z. Wang, J. Wang, Z. He, Z. Zheng, J. W. Y. Lam, B. Z. Tang, *Advanced Functional Materials* **2022**.

[13] J. Qian, B. Z. Tang, *Chem* **2017**, *3*, 56-91.

[14] aX. Liu, C. Zhu, B. Z. Tang, *Acc Chem Res* **2022**, *55*, 197-208; bA. Lal Koner, D. Chopra, N. T. Patil, *Chembiochem* **2022**, *23*, e202200320.

[15] W. Yin, Z. Yang, S. Zhang, Y. Yang, L. Zhao, Z. Li, B. Zhang, S. Zhang, B. Han, H. Ma, *Materials Chemistry Frontiers* **2021**, *5*, 2849-2859.

[16] C. Chen, R. Zhang, J. Zhang, Y. Zhang, H. Zhang, Z. Wang, X. Huang, S. Chen, R. T. K. Kwok, J. W. Y. Lam, D. Ding, B. Z. Tang, *CCS Chemistry* **2022**, *4*, 2249-2257.

[17] K. Hasrat, X. Wang, Y. Li, L. Yang, Y. Zhao, K. Xue, X. Wang, J. Deng, J. Liang, Z. Qi, *Dyes and Pigments* **2023**, *211*.

[18] aW. Li, M. Huang, Y. Li, Z. Yang, J. Qu, *Dyes and Pigments* **2021**, *186*; bY. Yang, J.-j. Tian, L. Wang, Z. Chen, S. Pu, *Journal of Photochemistry and Photobiology A: Chemistry* **2022**, *429*; cY. Zhou, Z. Yang, Z. Qiu, N. Tang, D. Sun, B. Liu, X. Wu, S. Ji, W.-C. Chen, Y. Huo, *Journal of Photochemistry and Photobiology A: Chemistry* **2022**, *428*; dJ. Ni, Y. Wang, H. Zhang, J. Z. Sun, B. Z. Tang, *Molecules* **2021**, *26*; eM. Sathiyaraj, V. Thiagarajan, *RSC Adv* **2020**, *10*, 25848-25855.

[19] H. Zhang, J. Liu, L. Du, C. Ma, N. L. C. Leung, Y. Niu, A. Qin, J. Sun, Q. Peng, H. H. Y. Sung, I. D. Williams, R. T. K. Kwok, J. W. Y. Lam, K. S. Wong, D. L. Phillips, B. Z. Tang, *Materials Chemistry Frontiers* **2019**, *3*, 1143-1150.